Tectonophysics, 211 (1992) 115–134
Elsevier Scienee Publishers B.V., Amsterdam

Earthquake nucleation on faults with rate- and state-dependent strength

James H. Dieterich

U.S. Geological Survey, 345 Middlefield Road, Menlo Park, CA 94025, USA

(Received June 7, 1991; revised version accepted November 26, 1991)

ABSTRACT

Dieterich, J.H., 1992. Earthquake nucleation on faults with rate- and state-dependent strength. In: T. Mikumo, K. Aki, M. Ohnaka, L.J. Ruff and P.K.P. Spudich (Editors), Earthquake Source Physics and Earthquake Precursors. *Tectonophysics*, 211: 115–134.

Faults with rate- and state-dependent constitutive properties reproduce a range of observed fault slip phenomena including spontaneous nucleation of slip instabilities at stresses above some critical stress level and recovery of strength following slip instability. Calculations with a plane-strain fault model with spatially varying properties demonstrate that accelerating slip precedes instability and becomes localized to a fault patch. The dimensions of the fault patch follow scaling relations for the minimum critical length for unstable fault slip. The critical length is a function of normal stress, loading conditions and constitutive parameters which include D_c, the characteristic slip distance. If slip starts on a patch that exceeds the critical size, the length of the rapidly accelerating zone tends to shrink to the characteristic size as the time of instability approaches. Solutions have been obtained for a uniform, fixed-patch model that are in good agreement with results from the plane-strain model. Over a wide range of conditions, above the steady-state stress, the logarithm of the time to instability linearly decreases as the initial stress increases. Because nucleation patch length and premonitory displacement are proportional to D_c, the moment of premonitory slip scales by D_c^3. The scaling of D_c is currently an open question. Unless D_c for earthquake faults is significantly greater than that observed on laboratory faults, premonitory strain arising from the nucleation process for earthquakes may by too small to detect using current observation methods. Excluding the possibility that D_c in the nucleation zone controls the magnitude of the subsequent earthquake, then the source dimensions of the smallest earthquakes in a region provide an upper limit for the size of the nucleation patch.

Introduction

The processes and interactions that lead to the initiation of unstable earthquake fault slip are collectively defined here as earthquake nucleation. This subject bears upon several topics of interest for earthquake seismology. In particular, earthquake nucleation determines the time of occurrence and place of origin of earthquakes. In turn, seismicity rates and space–time patterns of earthquakes represent selected characteristics of populations of nucleation events. Because earthquake nucleation processes may result in measurable physical changes prior to earthquakes, such as premonitory creep, this subject could also be of considerable relevance for earthquake prediction. Finally, nucleation processes might affect earthquake rupture propagation and seismic radiation by altering conditions along the fault prior to an earthquake.

The nucleation of earthquake slip may be influenced by several factors including fault constitutive properties, bulk properties of the rock mass in which an earthquake fault is embedded, stressing history, pore fluid interactions, and geometry of the fault-rock mass system. The following treatment examines details of the nucleation process on faults with a rate- and state-dependent constitutive law for fault slip, subjected to simple

Correspondence to: J.H. Dieterich, U.S. Geological Survey, 345 Middlefield Road, Menlo Park, CA 94025, USA.

stressing histories. Heterogeneity of physical conditions along a fault is also considered.

This study extends and generalizes the analyses of Dieterich (1986, 1987) which treat nucleation in response to constant-rate loading and loading with a periodic component. The previous studies relied upon numerical solutions of a simple spring and slider approximation of fault interactions. Below, an analytic solution for that problem is presented. In addition, the nucleation process is examined in detail with a plane-strain numerical model. The numerical model permits evaluation of simplifying assumptions used for the spring and slider approximation of fault interactions

Constitutive law

Constitutive laws with rate- and state-dependence successfully represent the experimental observations of ubiquitous velocity-, time-, and displacement-dependence of fault strength (Dieterich, 1979, 1981a; Ruina, 1983; Weeks and Tullis, 1985; Tullis and Weeks, 1986; Okubo and Dieterich, 1986; Biegel et al., 1989). In addition to representing experimental observations, this constitutive approach has the property of generating spontaneous slip instabilities under appropriate conditions with subsequent 'healing' of the fault to recover the loss of strength at the time of the instability. Tse and Rice (1986) have applied the constitutive law to model the earthquake cycle on strike slip faults and Stuart (1988) has employed it to model great subduction earthquakes in Japan. Conditions governing the onset of slip instability in simple spring and slider systems have been considered by Dieterich (1978, 1979, 1981a), Rice and Ruina (1983), Ruina (1983), Gu et al. (1984), Blanpied and Tullis (1986) and Tullis and Weeks (1986).

The sliding resistance, τ, divided by normal stress, σ, defines the coefficient of fault friction, μ:

$$\mu = \tau/\sigma \tag{1}$$

Throughout the following, σ is assumed to be constant.

Several similar, essentially equivalent, formulations of rate- and state-dependent fault strength have been employed. The previous nucleation studies (Dieterich, 1986, 1987) employ:

$$\mu = \mu_0 - A \ln\left(\frac{a}{\dot{\delta}} + 1\right) + B \ln\left(\frac{\theta}{b} + 1\right) \tag{2}$$

where, μ_0, A, B, a, and b, are experimentally determined parameters and δ, $\dot{\delta}$ and θ are fault slip, slip speed and the state variable, respectively. At $\dot{\delta}$ and θ well-removed from the rate limits (i.e. $a/\dot{\delta} \gg 1$, $\theta/b \gg 1$), eq. 2 simplifies to:

$$\mu = \mu_0' + A \ln \dot{\delta} + B \ln \theta \tag{3}$$

where μ_0' collects the constant terms from eq. 3:

$$\mu_0' = \mu_0 - A \ln a - B \ln b \tag{4}$$

The simplified form of the constitutive law is equivalent to that proposed by Ruina (1980, 1983) and later used by several other investigators. In eq. 3 the $\ln \theta$ term is sometimes replaced by $\Theta = \ln \theta$. Constants A and B typically have values in the range 0.005 to 0.010.

Sliding history effects and consequently displacement- and time-dependent effects are represented by the variable θ. Dieterich (1979) and Dieterich and Conrad (1984) interpret θ as a measure of the average age of load-supporting contacts between sliding surfaces and that contacts strengthen with age. Because contacts are destroyed and created during slip, it is reasoned that θ depends on the slip history. The following law for the evolution of θ with time or displacement has been discussed by Ruina (1980) and employed by Dieterich (1986):

$$\frac{d\theta}{dt} = 1 - \frac{\theta\dot{\delta}}{D_c}, \text{ or equivalent } \frac{d\theta}{d\delta} = \frac{1}{\dot{\delta}} - \frac{\theta}{D_c} \tag{5}$$

Displacement-dependent effects in experiments and in eq. 5 scale by the characteristic slip distance, D_c. In experiments, the magnitude of D_c depends on surface roughness and varies from about 3 microns for slip on initially bare, finely ground surfaces to a maximum of about 50 microns for coarsely ground surfaces separated by a layer of fault gouge (Dieterich, 1979, 1981a).

Note from eq. 5 that at steady-state, $d\theta/dt = 0$, and $\theta = D_c/\dot{\delta}$. When not at steady-state, θ tends

to evolve toward the steady-state value. At constant $\dot{\delta}$, eq. 5 has the solution:

$$\theta = \frac{D_c}{\dot{\delta}} + \left(\theta_0 - \frac{D_c}{\dot{\delta}}\right) e^{-\delta/D_c} \quad (6)$$

where θ_0 is the value of θ at $\delta = 0$. For a fault that is locked ($\dot{\delta} = 0$), $d\theta/dt = 1$ and θ increases with elapsed time. Because rapid slip and large displacements of an earthquake will reset θ to values approaching zero, a fault that has remained locked since the previous earthquake will have θ approaching the time interval from the last earthquake. Note, however, that the constitutive law as presented in eqs. 2 and 3 does not permit zero slip speed. Hence, small displacements in the interval between instabilities will tend to reduce θ to values somewhat less than the elapsed time interval.

For completeness, it is noted that an alternate evolution law has been used in several studies (Tse and Rice, 1986; Tullis and Weeks, 1986; Stuart, 1988). It may be written as:

$$\frac{d\theta}{d\delta} = \left(\frac{-\theta}{D_c}\right) \ln\left(\frac{\theta\dot{\delta}}{D_c}\right) \quad (7)$$

Use of evolution equation 7, in most cases, yields results that are similar to results with eq. 5. This study employs evolution equation 5, but a few comparisons with eq. 7 are made below.

Two special cases of the constitutive law are useful for the following discussion. The first is for steady-state sliding. At steady state, substitution of, $\dot{\delta} = D_c/\theta$, in eq. 2 yields the steady-state fault friction in terms of state:

$$\mu_s = \mu_0 - A \ln\left(\frac{a\theta}{D_c} + 1\right) + B \ln\left(\frac{\theta}{b} + 1\right) \quad (8)$$

Similarly, a substitution of $\theta = D_c/\dot{\delta}$ gives the steady-state fault friction as a function of $\dot{\delta}$. Under conditions where $a/\dot{\delta} \gg 1$, $\theta/b \gg 1$, the steady-state friction from the simplified friction law (eq. 3) is:

$$\mu_s = \mu_0' + A \ln D_c + (B - A) \ln \theta \quad (9)$$

The second case defines the upper limit of frictional strength for eq. 3 which occurs when $\dot{\delta} \to \infty$:

$$\mu_{max} = \mu_0 + B \ln\left(\frac{\theta}{b} + 1\right) \quad (10)$$

With the simplified form of the constitutive law (eq. 3), μ_{max} cannot be defined using $\dot{\delta} \to \infty$, because any frictional stress can be achieved by sliding at a suitable rate. A limiting slip speed, $\dot{\delta}_1$, for quasi-static slip is employed to define μ_{max}. If $\dot{\delta}$ increases to $\dot{\delta}_1$, then an instability is assumed to be have begun and quasi-static analysis is no longer appropriate. Hence, the maximum, quasi-static limit for the simplified constitutive law is

$$\mu_{max} = \mu_0' + A \ln \dot{\delta}_1 + B \ln \theta \quad (11)$$

If $\dot{\delta}_1 = a$, then μ_{max} defined in eq. 10 is the same value as that defined for eq. 11.

At stresses between μ_s and μ_{max}, fault slip is faster than the steady-state speed. Hence, θ decreases and, at constant $\dot{\delta}$, the fault weakens with time and displacement. At stresses below μ_s, the slip speed is less than steady state and the fault strengthens or 'heals'. As stress reaches μ_{max}, $\dot{\delta}$ equals $\dot{\delta}_1$ and unstable sliding commences.

Dieterich (1979, 1981a, 1986), Koslov and Liu (1980) and Gu et al. (1984) show that self-driven acceleration of slip speed to instability can occur in the stress range $\mu_s < \mu < \mu_{max}$ (see Fig. 1). This study is concerned with the processes and

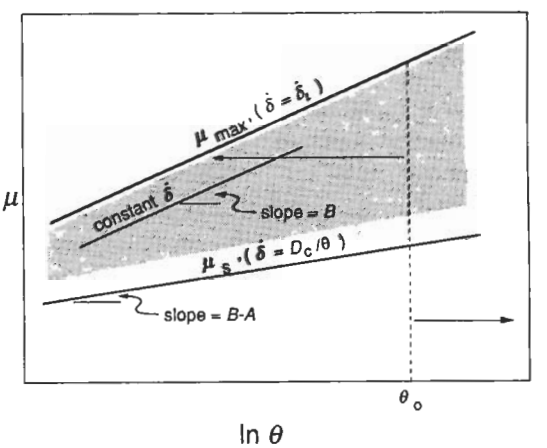

Fig. 1. Plot of friction coefficient against state, θ. Lines of constant slip speed and μ_{max}, which is defined at $\dot{\delta} = \dot{\delta}_1$, have slope B. The steady-state friction, μ_s, has the slope $B - A$. At stresses below μ_s, θ evolves to the right, increasing the strength of the fault at any reference slip speed. At stresses above μ_s, θ evolves to the left, decreasing the strength. Note that μ_s and μ_{max} change as θ evolves. The shaded portion of the graph schematically represents the region where the simplifying assumption employed for the simple patch solution, discussed below, is valid.

interactions that take place in this stress interval, where under suitable conditions, slip instability may nucleate. In general, for simulation of earthquake processes, θ will always be very large throughout the nucleation process insuring that the condition $\theta/b \gg 1$ is satisfied. Also, the condition $a/\dot{\delta} \gg 1$ holds until the stresses approach μ_{max}. At that point, the slip speeds are very high relative to D_c/θ, and the system is essentially at instability. Below, analytic solutions for a simple nucleation model and detailed plane-strain numerical solutions using simplified constitutive relations (eq. 3) are presented. Comparison with numerical solutions using the full constitutive formulation (eq. 2) shows the solutions differ only in the final moments immediately preceding instability and that those differences are slight.

Previous studies of the conditions for instability

Several studies of spring and slider systems (Dieterich, 1979, 1981a; Rice and Ruina, 1983; Ruina, 1983; Gu et al., 1984) have established that for an instability to occur, the stiffness ($k = \Delta\tau/d$) of the system must be less than some critical value, k_{crit} given by:

$$k_{crit} = \frac{\xi\sigma}{D_c} \tag{12}$$

where ξ is a parameter that depends upon the constitutive parameters and stress state. At stiffness greater than k_{crit}, displacements decrease the applied stress sufficiently to move the applied stress away from μ_{max}, terminating the slip acceleration. A dependence of the transition from stable sliding to stick slip, of the form given by eq. 12, has been established experimentally (Dieterich, 1978). Ruina (1983) and Rice and Ruina (1983) show that perturbations from steady-state slip will grow to instability for stiffness less than the critical stiffness where:

$$\xi = B - A \tag{13}$$

Hence, from eq. 12, the usual condition for instability is that $B > A$, which corresponds to steady-state velocity weakening. The value of ξ given by eq. 13 is a lower bound. For finite perturbations from μ_s, instability may occur with stiffness greater than that obtained from eq. 12 using eq. 13 (Rice and Gu, 1983).

An approximate representation of conditions required for onset of slip instability on a fault patch embedded in an elastic medium is found by combining the spring and slider results with elasticity solutions for displacement along a crack (Dieterich, 1986). This assumes that properties and conditions at the center of the patch are representative of the entire patch. The approximate effective stiffness of a fault patch is obtained from crack solutions relating fault slip δ to stress drop $\Delta\tau$:

$$k = \frac{\Delta\tau}{\delta} = \frac{G\eta}{l} \tag{14}$$

where l is the half length (or radius) of the fault patch, G is the shear modulus (Poisson's ratio taken to be 0.25) and η is a factor with a value that depends upon the geometry of the slip patch and assumptions relating to slip or stress conditions on the patch. Table 1 gives values of η for some simple patch geometries.

TABLE 1

Values [a] of η for different patch geometries

η	l	Patch	Reference
$7\pi/24$	radius	circular crack	Eshelby (1957)
$2/3$	length/2	plane strain, constant shear stress	Starr (1928)
$4/3\pi$	length/2	plane strain, constant displacement	Chinnery (1969)
$1/2$	length/2	anti-plane strain, constant shear stress	Knopoff (1958)
$1/\pi$	length/2	anti-plane strain, constant displacement	Chinnery (1969)

[a] Assumes Poisson's ratio $\nu = 0.25$. Displacement δ is measured at the center of the crack.

Dieterich (1986) combines the relation for critical stiffness for instability (eq. 12) with the relation for patch stiffness (eq. 14) to obtain:

$$l_c = \frac{G\eta D_c}{\xi\sigma} \tag{15}$$

where l_c is the minimum patch half-length for unstable fault slip. Patches with dimensions less than $2l_c$ will have stiffnesses in excess of k_{crit} and sliding will always be stable. Equation 15 implies a lower bound for the dimensions of the earthquake source. Examination of stick-slip events along a 2-m fault provided an approximate experimental verification of this relationship (Dieterich, 1981b). In that study, stick-slip events, confined to the interior of the fault were observed, and the dimensions of the unstable fault patch always exceeded the approximate minimum size predicted for the conditions of the experiment.

Simple patch model

The simplified nucleation model consists of a fault patch embedded in an elastic body. The patch dimensions are fixed and conditions along the fault are represented by the center-point values. Stress acting on the patch is controlled by remote displacements and by slip on the patch. Remote stressing (e.g. tectonic loading, earth tides or stress transfer by slip elsewhere on the fault) results in a stress change on the patch in the absence of slip on the patch. The patch has dimensions equal to or in excess of $2l_c$ as given by eq. 15 and has an effective stiffness k, from eq. 14.

Equating the constitutive law (eq. 3) with fault stress gives:

$$\frac{\tau(t) - k\delta}{\sigma} = \mu_0' + A \ln \dot{\delta} + B \ln \theta \tag{16}$$

where $\tau(t)$ is the remotely applied stress acting on the fault in the absence of slip and $-k\delta$ is the decrease in stress due to fault slip. Using eq. 16 with the evolution law for θ, the problem may be solved numerically.

However, when the nucleation process is under way and slip is accelerating, the slip speed is much greater than the steady-state speed ($\dot{\delta} \gg D_c/\theta$). Under these conditions ($\dot{\delta} \gg D_c/\theta$), the $1/\dot{\delta}$ term in eq. 5 does not contribute to the evolution and eq. 5 reduces to:

$$\frac{d\theta}{d\delta} = -\frac{\theta}{D_c}, \quad \theta = \theta_0 e^{-\delta/D_c} \tag{17}$$

Hence, under these conditions, θ evolves toward an ever diminishing steady state ($\theta = D_c/\dot{\delta}$) that is effectively zero compared to the current θ and the evolution becomes independent of slip speed. This condition holds once the nucleation process is under way, as the slip undergoes acceleration to instability. The following analysis employs the approximate relationship 17 for evolution of θ. Conditions under which this approximation is appropriate are discussed in greater detail below.

Substitution of eq. 17 into eq. 16 yields:

$$\frac{\tau(t) - k\delta}{\sigma} = \mu_0' + A \ln \dot{\delta} + B \ln \theta_0 - \frac{B\delta}{D_c} \tag{18}$$

A variety of functions for the remote stressing, $\tau(t)$, result in a separable differential equation that may be solved directly. For the simple case of constant rate of remote loading, $\tau(t) = \tau_0 + \dot{\tau}t$, (eq. 18) yields:

$$C\int_0^t \exp\left(\frac{\dot{\tau}t}{A\sigma}\right) dt = \int_0^\delta \exp\left(\frac{-H\delta}{A}\right) d\delta \tag{19}$$

where C and H contain terms for the initial conditions and model constants, respectively:

$$C = \frac{D_c}{\theta_0} \exp\left(\frac{\tau_0/\sigma - \mu_s}{A}\right) = \dot{\delta}_0 \tag{20}$$

$$H = \frac{B}{D_c} - \frac{k}{\sigma} \tag{21}$$

Note in eq. 20 that C is found to be the initial slip speed, $\dot{\delta}_0$. Equation 19 has the following solutions:

$$\delta = \frac{-A}{H} \ln\left\{\frac{CH\sigma}{\dot{\tau}}\left[1 - \exp\left(\frac{\dot{\tau}t}{A\sigma}\right)\right] + 1\right\}, \quad \dot{\tau} \neq 0 \tag{22}$$

$$\delta = \frac{-A}{H} \ln\left\{1 - \frac{CHt}{A}\right\}, \quad \dot{\tau} = 0 \tag{23}$$

The slip speeds are:

$$\dot{\delta} = \left\{ \left[\frac{1}{C} + \frac{H\sigma}{\dot{\tau}} \right] \left[\exp\left(\frac{-\dot{\tau} t}{A\sigma} \right) \right] - \frac{H\sigma}{\dot{\tau}} \right\}^{-1}, \quad \dot{\tau} \neq 0 \tag{24}$$

$$\dot{\delta} = \left[\frac{1}{C} - \frac{Ht}{A} \right]^{-1}, \quad \dot{\tau} = 0 \tag{25}$$

The time of instability, t_i, is obtained by substituting $\dot{\delta}_i$, the assumed slip speed at the start of instability, into eqs. 24 and 25:

$$t_i = \frac{A\sigma}{\dot{\tau}} \ln\left(\frac{1}{C} + \frac{H\sigma}{\dot{\tau}} \right) - \frac{A\sigma}{\dot{\tau}} \ln\left(\frac{1}{\dot{\delta}_i} + \frac{H\sigma}{\dot{\tau}} \right), \quad \dot{\tau} \neq 0 \tag{26}$$

$$t_i = \frac{A}{H} \left(\frac{1}{C} - \frac{1}{\dot{\delta}_i} \right), \quad \dot{\tau} = 0 \tag{27}$$

In turn, expressions for the total displacement at the time of instability may be obtained by substituting t_i into eqs. 22 and 23. State θ, at t_i is then obtained from the total displacement using eq. 17.

If the stiffness of the patch is sufficiently high, then the rate of stress decrease due to slip will result in decelerating slip. In the μ vs. ln θ plane, lines of constant slip speed have the slope B. Hence, slip will accelerate if:

$$\frac{d\mu}{d \ln \theta} < B \tag{28}$$

See Figure 1. The derivative, $d\mu/d \ln\theta$, is found from the solutions for displacement with eq. 18. Equating $d\mu/d \ln\theta$ to B gives the patch stiffness that results in constant slip speed:

$$k_{crit} = \frac{B\sigma}{D_c} + \frac{\dot{\tau}}{C} \tag{29}$$

Slip will accelerate for stiffnesses less than k_{crit}. In eq. 29, if $\dot{\tau} = 0$, or if C is large compared to $\dot{\tau}$ (large $\dot{\delta}_0$), then $k_{crit} = B\sigma/D_c$ (i.e. $\xi = B$). Note that parameter A does not appear, and that acceleration to instability may occur on faults with a positive steady-state slip speed dependence ($A - B > 0$). However, the displacement during unstable slip may be quite small, because θ will soon evolve to steady-state, velocity strengthening, which will stabilize the slip.

These results alone are insufficient to determine if an instability will nucleate. In particular, the condition required for this solution, $\dot{\delta} \gg D_c/\theta$, may be satisfied initially, but evolution due to slip may result in this condition later being violated. A particular solution may be easily checked to insure that it does not violate this condition by solving for θ_i at the time of instability and testing to see if it remains large compared to $D_c/\dot{\delta}_i$.

Numerical model

The purpose of the numerical model is to investigate the nucleation process in more detail and without the simplifying constraints imposed for the simple patch solutions. Hence, the numerical model employs the constitutive relations, eqs. 2 or 3 and the full evolution eqs. 5 or 7. The model assumes plane-strain interactions of an array of fault dislocations (Fig. 2). The medium is homogeneous, elastic and infinite. The fault is assumed to be initially planar. A section of fault is free to slip and beyond the ends of the model, the fault is pinned. The model and preliminary results for nucleation were first reported by Dieterich (1988).

For this study, constitutive parameters A, B and D_c are the same at all points on the fault. Shear stress, fault slip and θ are free to vary with

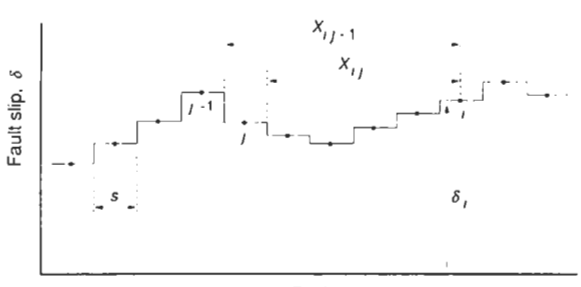

Fig. 2. Representation of fault slip in numerical model. The fault is divided into discrete segments of length s. Fault slip on a segment is constant and segments are bounded by elastic dislocations. Stress at the mid-point of segment i, due to slip on segment j, is found from the elastic dislocations bounding segment j, at distances X_{ij-1} and X_{ij}.

time and position. Normal stress remains constant during slip, but each point may be assigned different normal stresses to give spatial variation of fault strength.

An array of n equally spaced segments, bounded by dislocations, provides a descretized representation of slip distribution and stress state along the fault patch. Slip along each segment is constant. At time t, the stress at node i, located at the center of segment i, is given by:

$$\tau_i = \tau_i^0 + \dot{\tau} t + \Delta\tau_i \tag{30}$$

where τ_i^0 is the initial stress on the segment at time $t = 0$, $\dot{\tau}$ is a constant, remote stressing rate, and $\Delta\tau_i$ is the change of stress resulting from displacements of the fault nodes. $\Delta\tau_i$ is given by the system of equations:

$$\Delta\tau_i = S_{ij}\delta_j, \quad i, j = 1, 2, \ldots, n \tag{31}$$

where eq. 31 employs summation convention and δ_j is the array of nodal displacements giving total fault slip. The n by n array of coefficients relating stress to displacement, S_{ij}, is obtained from elastic dislocation solutions. For an array of dislocation segments bounded by edge dislocations in an infinite medium:

$$S_{ij} = \frac{G}{2\pi(1-\upsilon)}\left[\frac{1}{X_{ij}} - \frac{1}{X_{ij-1}}\right] \tag{32}$$

where G and ν are shear modulus and Poisson's ratio, respectively. The terms X_{ij} and X_{ij-1} are distances from the center of segment i to the two dislocations bounding segment j (see Fig. 2). For uniform dislocation spacing, s:

$$X_{ij} = s[i - j - 1/2]$$

$$X_{ij} = s[i - j + 1/2] \tag{33}$$

Expressions for anti-plane strain, employing screw dislocations at the segment boundaries are identical to eq. 32 except that Poisson's ratio, ν, is omitted. Equations for a vertical fault with a free surface in anti-plane strain, or faults with a mirror symmetry plane perpendicular to the center of the fault, are analogous to eq. 32 except that added distance terms are required for the image segments.

A time marching procedure follows the slip of each node and evolution of friction up to the time that the first segment becomes unstable. Constant slip speed during a time step is assumed. For each time step, the computation finds the slip speed at every fault node such that, at the midpoint of the time step, the frictional resistance on a segment, τ_f, is equal to the applied stress on the segment, τ_e. The nodal slip speeds that satisfy this condition are simultaneously determined iteratively, using a predictor–corrector method. Every iteration begins with a trial τ_f^k, where k indicates the k-th iteration. The first iteration begins with τ_f^1 set equal to the known nodal stress at the beginning of the step obtained from eq. 31. The trial slip speed, $\dot{\delta}_{\text{trial}}^k$, that yields a frictional resistance equal to τ_f^k at the midpoint of the step is calculated from the constitutive relations. This calculation employs the explicit constant $\dot{\delta}$ solution (eq. 6) of the evolution equation to evolve from the known value of θ at the beginning of the step. The nodal stresses at the midpoint of the time step, τ_e^k, are then calculated from eq. 31 using $\dot{\delta}_{\text{trial}}^k$ and the step duration Δt. If $|\tau_f^k - \tau_e^k| \geq \tau_{\text{error}}$, then another iteration is performed using $\tau_f^{k+1} = \tau_e^t$.

This method is numerically stable and easy to implement. For the simulations reported here, $\tau_{\text{error}} = 0.00005\sigma$ and the time step solution generally converges after 2 iterations. The solutions are insensitive to the size of the steps, provided $\Delta\delta \leq 0.1 D_c$ and provided $\Delta t \leq 0.5 A\sigma/\dot{\tau}$.

Results of numerical simulations

The simulations employ the simplified constitutive law (eq. 3) with evolution law eq. 5, unless specified otherwise. Also, unless specified, the stressing rate $\dot{\tau}$ is zero and the initial stress at the start of the simulation is set above the steady-state friction ($\tau^0 > \mu_s\sigma$) to insure self-driven acceleration of slip to instability. This is roughly equivalent to imposing a stress step that moves a previously locked fault across the steady-state boundary and into the field where creep instability begins. Several series of simulations were also performed with $\dot{\tau} \neq 0$ permitting the conditions to evolve across the steady-state boundary from below. In all simulations, initial θ_0 is 10^9 s (~ 31.7 years), Poisson's ratio is 0.25 and $G/\sigma = 10^4$.

Figure 3 illustrates results with uniform initial conditions and uniform normal stress. The fault patch consists of 299 nodes. Figures 3a–3c give profiles, at successive time steps, of slip speed, shear stress and displacement, respectively. The time steps are not constant, but decrease as the slip speed of the fastest node increases. In this example, every 50th time step is shown. Figure 3d

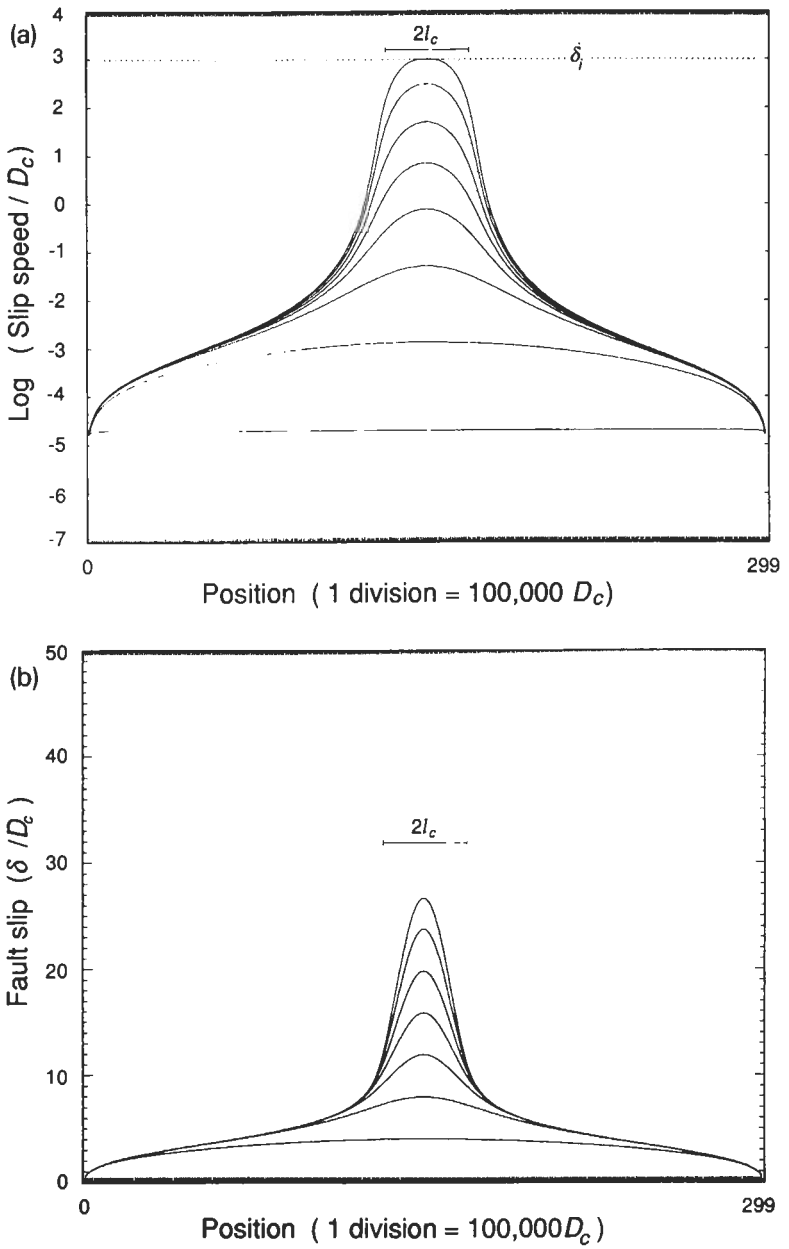

Fig. 3. Numerical model with 299 nodes (nodal spacing of 100,000 D_c) and uniform initial conditions. Parameters for the calculations are: $A = 0.008$, $B = 0.009$, $\theta = 10^9$ s, $G = 10^4$ s, $\dot{\tau} = 0$, and initial shear stress $\tau = (\mu'_0 + 0.1)\sigma$. (a), (b), (c) give the logarithm of slip speed, displacement and shear stress, respectively, as functions of position on fault. Position is scaled by D_c. The approximate width of the zone of accelerated slip, $2l_c$, is obtained from eq. 15 with $\xi = 0.4B$. (d) gives the slip at the center of the model. The vertical lines in (c) mark the maximum shear on the time-step profiles and illustrate the contraction of the most active portion of the crack with increasing time.

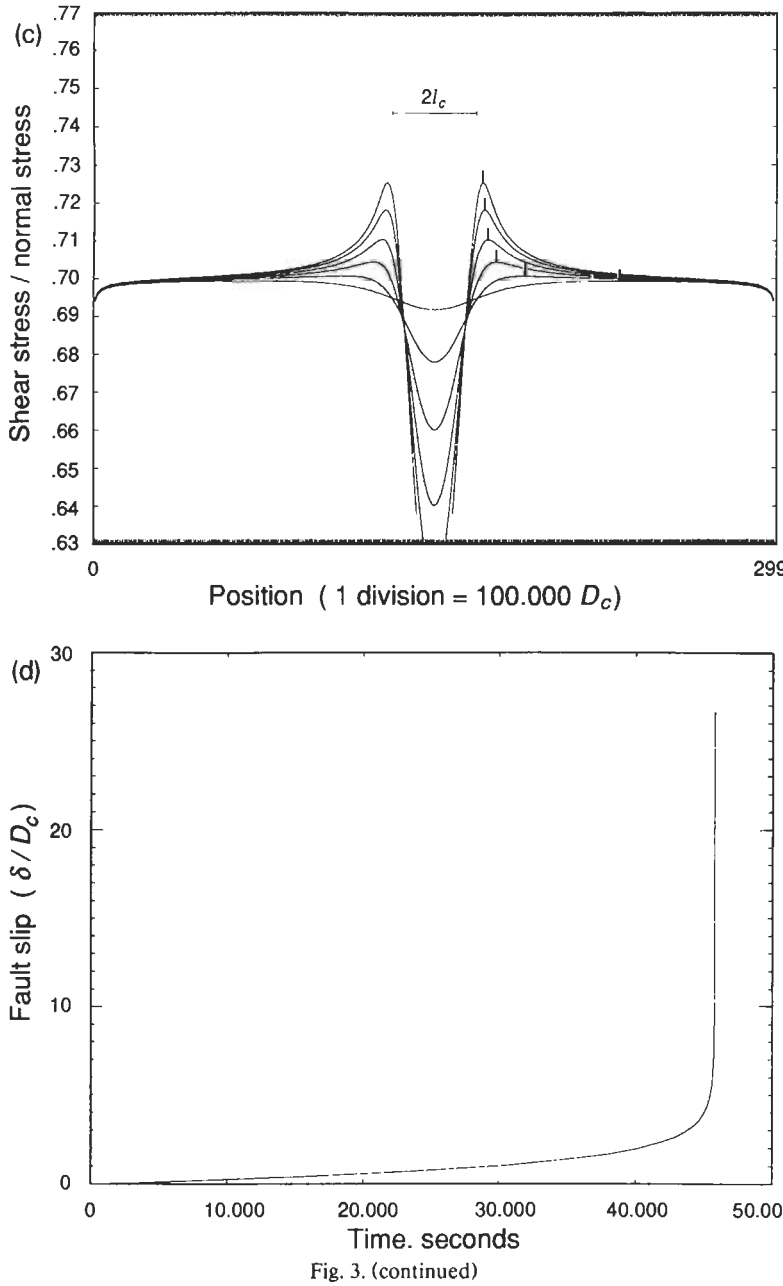

Fig. 3. (continued)

gives the displacement vs. time of the node at the center of the segment. This displacement history is characteristic of all simulations that reach the instability condition.

An interesting feature of the numerical model is that the most rapidly slipping portion of the fault patch constricts to a sub-patch (Figs. 3a and 3c). The development of a sub-patch is characteristic of simulations with plane strain or anti-plane strain. The length of the sub-patch correlates with the critical stiffness of eq. 29, i.e. $\xi = B$ in eq. 15. However, the length of the sub-patch at instability is always longer than the predicted minimum patch length, $2l_c$, obtained using $\xi = B$. A generally satisfactory empirical representation of the sub-patch half-length is obtained from eq. 15 using $\xi \sim 0.4B$. Figure 3 and the following figures show l_c from eq. 15 with $\xi = 0.4B$.

As suggested by eq. 29, the numerical results demonstrate that instabilities can nucleate when $A - B > 0$ (velocity strengthening), given sufficient perturbation of stress above the steady-state friction. Qualitatively, the simulations with $A - B > 0$ are similar to those with $A - B < 0$, including the development of a sub-patch with dimensions that scale by eq. 15 using $\xi = 0.4B$. However, if the fault is rate-strengthening, and if the initial stress is not sufficiently high relative to the steady-state friction, then accelerating slip terminates and the condition for instability is not reached.

Figure 4 illustrates results of models with uniform initial θ, uniform normal stress and random initial shear stress, distributed uniformly between

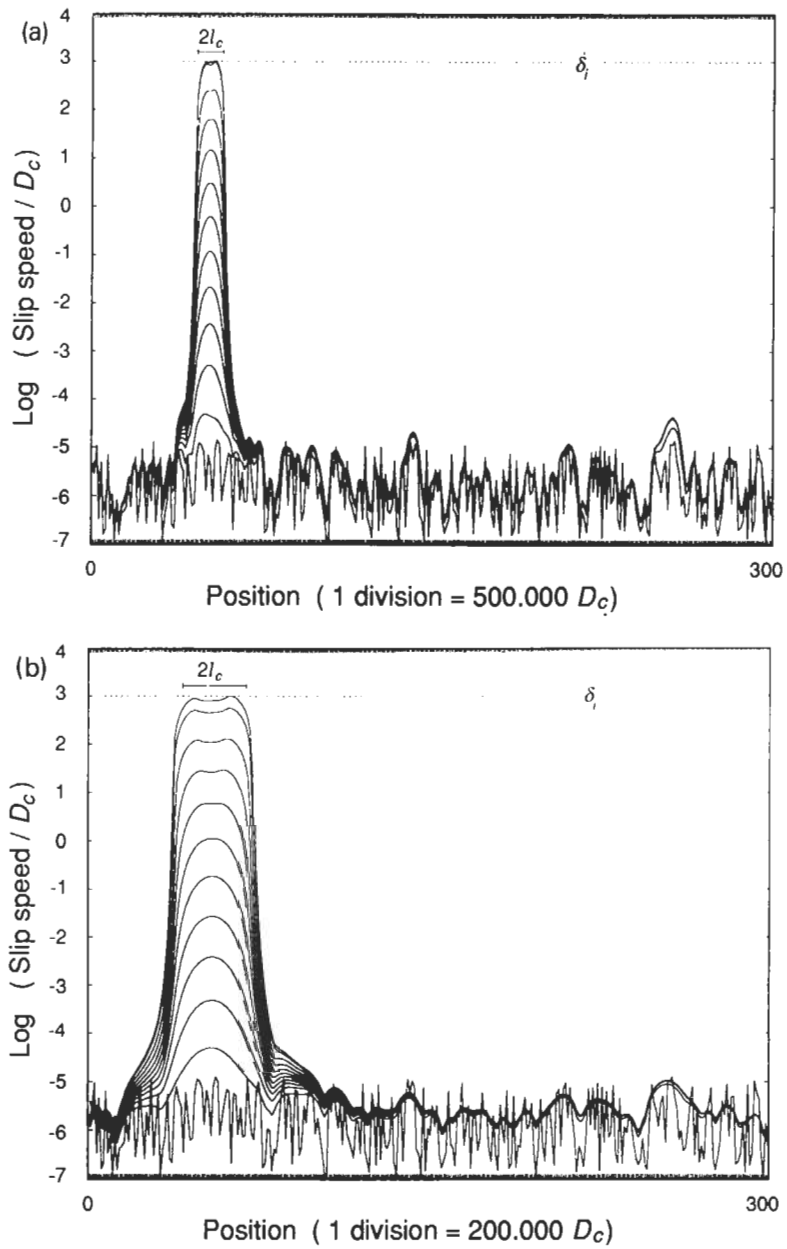

Fig. 4. Numerical model with 300 nodes and randomized initial shear stress. Parameters for the calculations are: $A = 0.004$, $B = 0.006$, $\theta = 10^9$ s, $G = 10^4\sigma$, $\dot{\tau} = 0$, and initial shear stress from $(\mu_0' + 0.06)\sigma$ to $(\mu_0' + 0.08)\sigma$. The logarithm of slip speed for faults with different values of D_c is indicated.

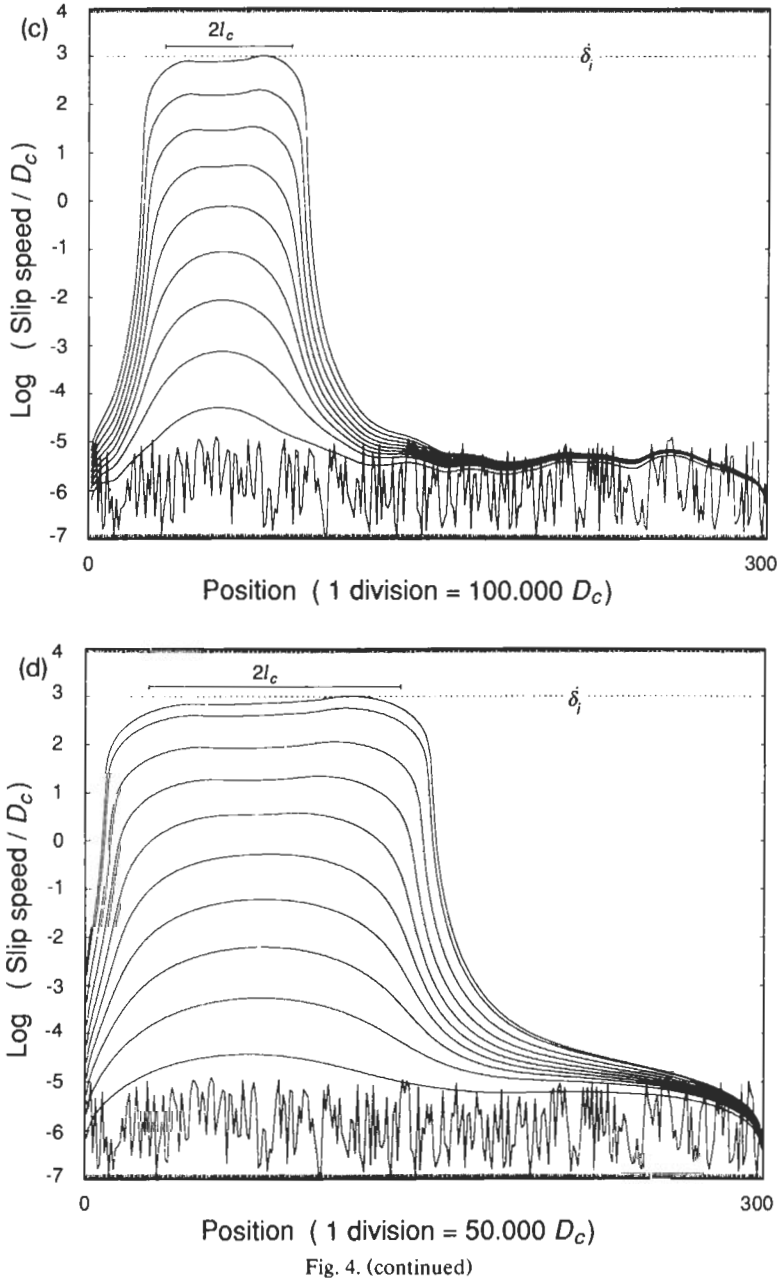

Fig. 4. (continued)

$\tau = (\mu'_0 + 0.06)\sigma$ and $\tau = (\mu'_0 + 0.08)\sigma$. Except for the magnitude of D_c, the parameters employed for the simulations of Figure 4 are identical ($A = 0.004$, $B = 0.006$, $\theta_0 = 10^9\sigma$). Because of the non-uniform initial stress, initial slip speeds are also non-uniform.

As with the uniform initial stress models, the dimensions of the unstable sub-patches in each heterogeneous stress model correlate with l_c of eq. 15 with $\xi = 0.4B$. Note, that each of the following examples employs different values of B and $A - B$ to establish that l_c scales by B and not by A or some combination of A and B. When D_c is varied, the zone of most rapid slip also changes according to eq. 15. Also, note in Figure 4 that the initial heterogeneity of slip speed quickly becomes smoothed at spatial wavelengths somewhat less than l_c. This is also reflected in an initial smoothing of the shear stress profiles. At longer wavelengths there is growth of

the slip speed heterogeneities. Because of the very rapid acceleration, the slip in one region soon outpaces the other areas of local acceleration.

Figure 5 gives an example of a simulation with uniform initial shear stress and uniform initial θ and heterogeneous normal stress randomly distributed between $\sigma = 0.95\bar{\sigma}$ and $\sigma = 1.05\bar{\sigma}$, where $\bar{\sigma}$ is the mean normal stress. For the models illustrated in Figure 5, different values of D_c were employed and the other parameters were the same ($A = 0.005$, $B = 0.008$, $\theta_0 = 10^9\sigma$). Again, B and $B - A$, for this set of simulations, differ from the values used for the models of

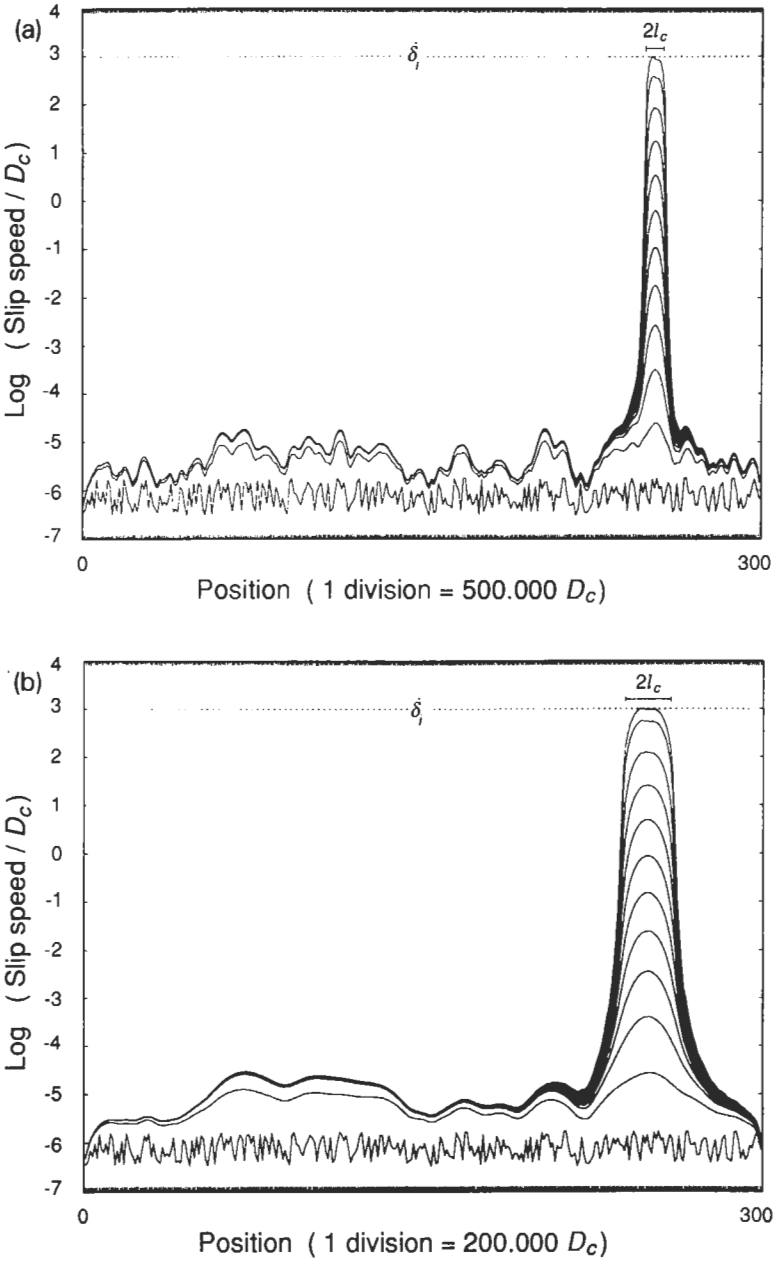

Fig. 5. Numerical model with 300 nodes and randomized normal shear stress and uniform initial shear stress. Parameters for the calculations are: $A = 0.005$, $B = 0.008$, $\theta = 10^9$ s, $G = 10^4\sigma$, $\dot{\tau} = 0$, uniform initial shear stress of $(\mu_0' + 0.095)\bar{\sigma}$ and normal stress from $\sigma = 0.95\bar{\sigma}$ to $\sigma = 1.05\bar{\sigma}$, where $\bar{\sigma}$ is the mean normal stress. The logarithm of slip speed for faults with different values of D_c is indicated.

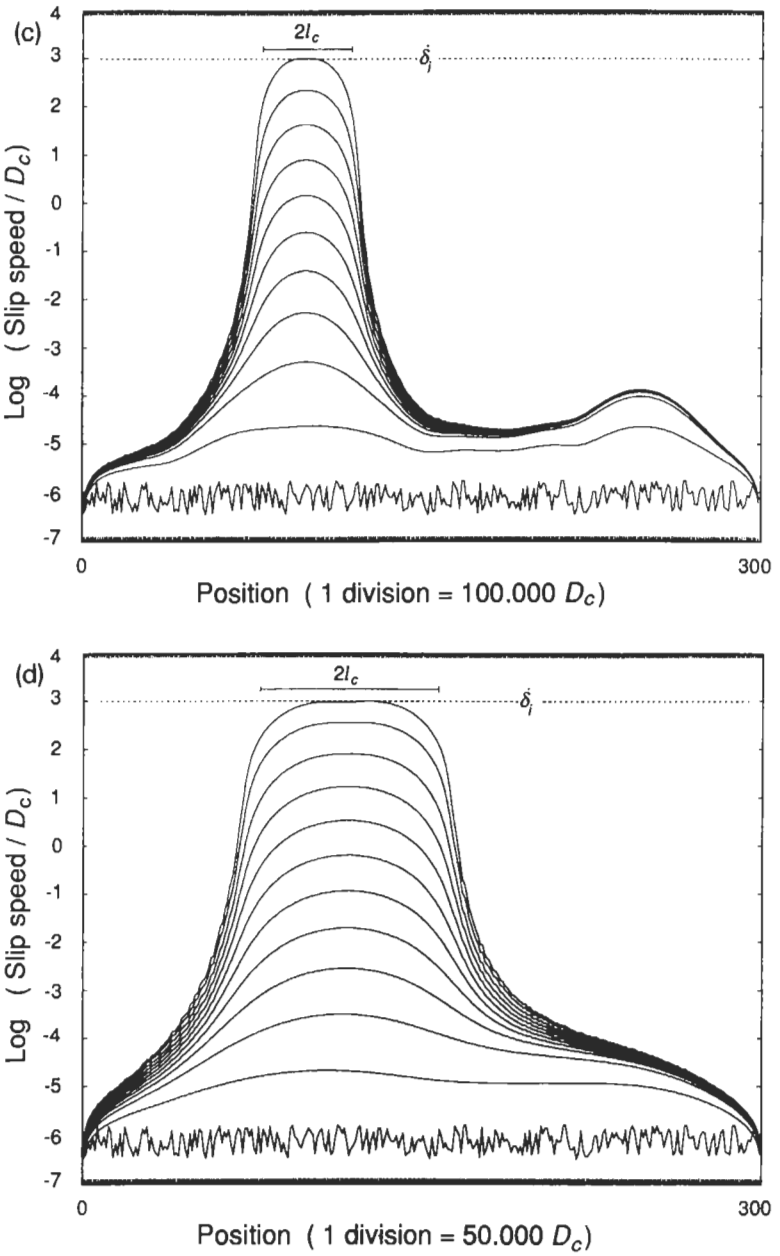

Fig. 5. (continued)

Figures 3 and 4. The results with heterogeneous normal stress are similar to the results obtained using heterogeneous shear stress. Spatial variations of slip speed at wavelengths less than l_c rapidly become smoothed and the sub-patch size at the onset of instability approximately equal to l_c with $\xi = 0.4B$.

The principal new finding, from the numerical models, is the development of a sub-patch that accelerates to instability. Attempts to force accelerated slip over longer lengths, by setting a higher initial shear stress along a longer patch, resulted in progressive constriction of the most rapidly slipping portion of the fault, with increasing displacement. Patch dimensions greater than l_c (with $\xi = 0.4B$) were observed under two circumstances. (1) The initial stress is close to μ_{max}. In this situation, it appears that instability occurs

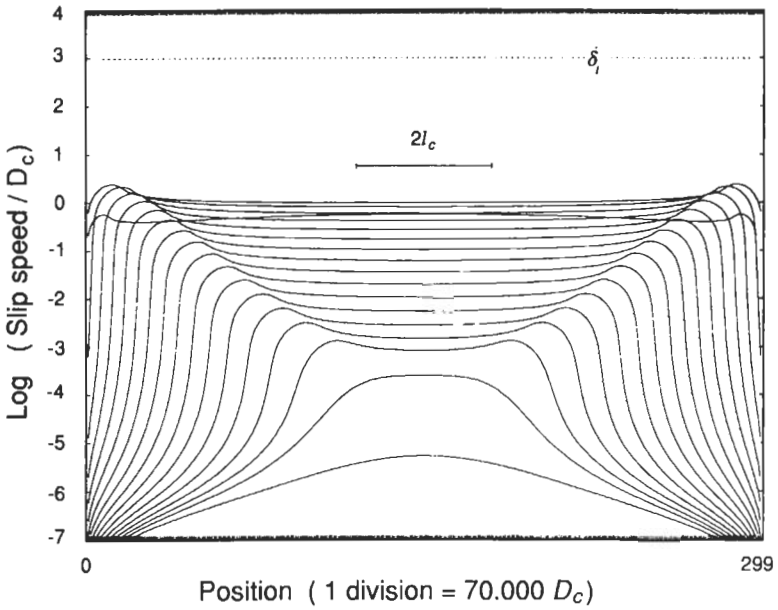

Fig. 6. Numerical model with 299 nodes showing spread of zone of rapid slip. Parameters for the calculations are: $A = 0.008$, $B = 0.009$, $\theta = 10^9$ s, $G = 10^4\sigma$, $\dot{\tau} = 0$, and uniform initial shear stress $\tau = (\mu_0' + 0.04)\sigma$. Initially, slip concentrates in a zone with half-length corresponding to eq. 15 with $\xi = 0.4B$, then begins to expand. When the zone of rapid slip reaches the ends of the model, slip begins to decelerate. The initial shear stress for this calculation is near the steady-state stress, 0.62σ. The critical length for unstable slip from steady-state sliding from eq. 15 and using $\xi = B - A$, is 190 divisions.

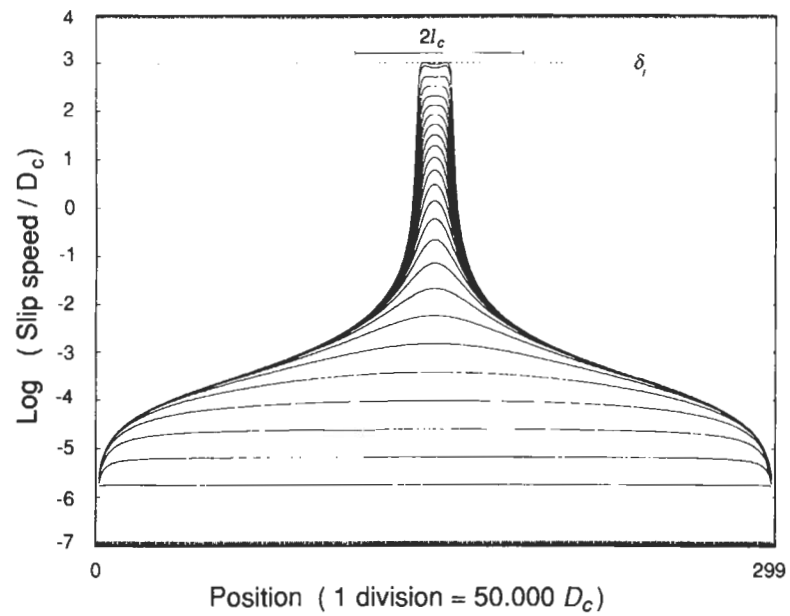

Fig. 7. Numerical model with 299 nodes and uniform initial conditions. This model employs alternative evolution equation 7 instead of eq. 5. Constitutive parameters for the calculations are identical to those of Figure 3, with $\dot{\tau} = 0$ and initial shear stress $\tau = (\mu_0' + 0.08)\sigma$. The length bar gives the width, $2l_c$, obtained from eq. 15, with $\xi = 0.4B$. Note that the dimension of the zone that nucleated slip is much less than that found using evolution law 5.

before sufficient slip can occur to permit development of the sub-patch. (2) Low initial stress, close to μ_s, with stressing rate at or near to zero. In this case, the most rapidly slipping zone constricts to a sub-patch, but then begins to enlarge with increasing slip. The lengthening appears to be related to the approach of θ to steady-state along the most rapidly sliding portion of the fault. Near steady-state, the critical stiffness for instability is given by $\xi = B - A$ instead of $\xi = B$. Hence the critical half-length for instability is greater near steady-state. In extreme cases, if the total length of the model is not much longer than l_c with $\xi = B - A$, the sub-patch expands to fill the slipping segment and the acceleration of slip stops (Fig. 6).

A limited series of results were obtained using the alternate evolution equation 7. Use of eq. 7 in these simulations yields results qualitatively similar to those discussed above. However, total premonitory displacements are smaller and the sub-patch is significantly narrower than that found in the models that used evolution equation 5 (see Fig. 7).

Comparison of numerical results with the simple model

The numerical results provide a test of the solutions for a simple patch and the simplifying assumptions that were employed.

Figure 8 compares the solutions for the time to instability from the simplified fault patch model (eqs. 26, 27) with times calculated using the 2D numerical model, assuming uniform initial stress. For this comparison, the patch stiffness, k, for the solution was evaluated using eq. 14 with l set equal to the half-length of the fault in the numerical model and $\eta = 2/3$, i.e. the factor for constant shear stress crack in plane strain (Table 1). Over the range of conditions illustrated in Figure 8, the times to instability given by the simple model generally differ from the corresponding numerical results (open symbols) by 2% or less. However, the patch solution diverges significantly from the numerical results for the case $\dot{\tau} = 0$ for initial stresses near μ_s. In this region, the numerical results form an asymptote to the μ_s line. This difference arises from a breakdown of the assumption $\dot{\delta} \gg D_c/\theta$, used for the patch solutions. The results for $\dot{\tau} \neq 0$, are in close agreement with the numerical model even for initial stresses substantially below μ_s, where the condition $\dot{\delta} \gg D_c/\theta$ is not satisfied. The success of the simple model in this range is apparently due to negligible evolution of θ as it is driven across the steady-state boundary by the external stressing, $\dot{\tau}$.

At stresses near μ_{max}, giving times to instability $\leqslant 10^{-2}$ s, the numerical results for the time to instability differ from the patch solutions by as much as 20%. The cause of this discrepancy is not known and has not been investigated as it seems of little practical interest.

A series of numerical results, using the full constitutive relation (eq. 2), with rate cut-offs, was obtained to evaluate the possible errors introduced through the use of the simplified constitutive relation (eq. 3) with the simple patch model. As suggested by the earlier discussion, for these problems where $\theta/b \gg 1$ is large, the results

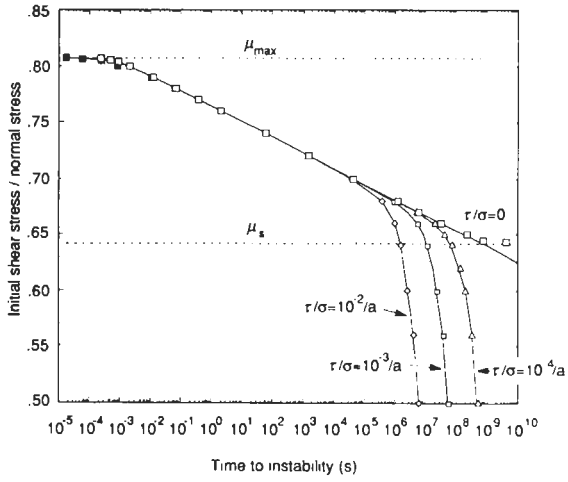

Fig. 8. Comparison of simple patch solution, continuous curves and numerical results (symbols) for time to instability. Parameters for the calculations are: $A = 0.008$, $B = 0.009$, $\mu'_0 = 0.6$, $\theta = 10^9$ s, $G = 10^4\sigma$. In the numerical model, the initial stress is uniform and the total half-length of the model is 2.5×10^7 D_c. The stiffness used for the patch solution was obtained from eq. 14 and used $l = 2.5 \times 10^7$ D_c. Open symbols give the numerical results using the simplified form of the constitutive law (eq. 3). At times to instability (of $\leqslant 10^{-1}$ s), the numerical results obtained using the full constitutive law (eq. 2), with $b = D_c$ /s, begin to diverge from the results obtained with eq. 3 (solid squares).

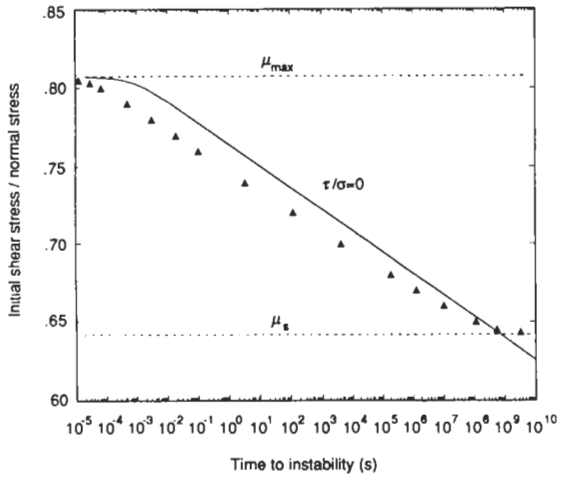

Fig. 9. Comparison of simple patch solution, continuous curves and numerical results for time to instability. In this example, the numerical results (triangles) were obtained using the alternative evolution equation (7). Parameters for the calculations are identical to those of Figure 8.

differ only in the region of μ_{max}, where the system is a very short time from instability. The solid squares in Figure 8 show the results using

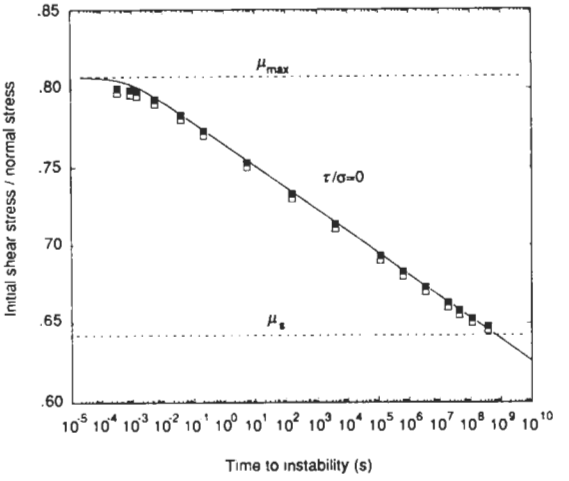

Fig. 10. Comparison of simple patch solution, continuous curves and numerical results for time to instability with heterogeneous initial shear stress. Parameters for the calculations are identical to those of Figure 8, except that initial shear stress varied randomly about the initial mean stress by $\pm 0.01\bar{\tau}$. Open squares plot the results using the mean initial shear over the entire fault, and the filled squares plot the results using the mean initial shear stress on the section of the fault that eventually nucleated the instability.

relation 2 with $b = 1.0\ D_c/s$. The maximum difference in the time to instability obtained using the different constitutive relations is about 0.01 s, which again seems of little practical interest.

The displacement given by eqs. 22 and 23 shows agreement with the numerical model that is comparable to that of the time-to-instability results. That is, the displacement of the center node of the numerical model at some time t, is equal to the displacement given by eq. 22 or 23 at time T, where $|(T-t)/T| < 0.02$. The characteristic form of the solution is well-represented by the numerical result of Figure 3d. The patch solutions diverge from the numerical results for initial stresses in the vicinity of μ_s, when the stressing rate is zero, because of a breakdown of the assumption $\dot{\delta} \gg D_c/\theta$.

Figure 9 compares the time to instability from the numerical model and using the alternate evolution equation 7 with the patch solutions. The results are qualitatively similar, but differ quantitatively.

Figure 10 compares the results for the model with heterogeneous initial stress with the patch solutions. In this comparison, the open symbols define the shear stress as the mean of the initial stresses over the entire fault. The agreement of the model with the patch solution (eq. 27) appears to be quite good, but the times from the numerical model are consistently less than those from eq. 27. This appears to be because the section of fault that nucleates the instability has a higher initial stress than the mean initial stress of the entire fault. Better agreement between the numerical results and the patch solution is obtained using the local mean of the initial stress on the section of the fault that nucleated the instability (solid symbols in Fig. 10).

Discussion

The extent to which the results presented here describe the earthquake nucleation process depends on the applicability of the rate- and state-constitutive formulation to faults in nature. This question cannot be answered definitively at this time, but several lines of evidence suggest that

faults have properties of the sort characterized by this formulation. First, controlled sliding experiments using laboratory faults have shown that the properties described by the rate- and state-dependent formulation are characteristic. Similar results are observed for bare faults and faults with gouge, under wet and dry conditions. Second, laboratory faults exhibit a rich variety of sliding phenomena, apparently analogous to faults in nature, that include steady creep, simple or chaotic oscillatory creep, and unstable slip that is preceded by an interval of accelerating creep. These sliding behaviors, and their transitions to other behaviors, have been modeled quantitatively, using rate- and state-dependent constitutive formulations. Third, this type of governing relation for fault strength has those properties that seem to be required of faults in nature, including slip weakening at the onset of unstable slip, instantaneous rate strengthening that is characteristic of rocks and spontaneous 'healing' that restores strength following unstable slip.

In view of these considerations it is argued that constitutive properties of the type discussed in this paper govern the earthquake nucleation process. However, the constitutive constants and functional descriptions may be poorly defined for the conditions and time scales characterizing the slip of faults in nature. For example, processes such as solution transport and cementation may enhance the healing rate, i.e. state-dependency, at longer time scales. Also the results obtained using different evolution equations, while qualitatively similar, differ quantitatively, further illustrating uncertainties in the formulation. Hence, the results presented here probably should be regarded as a plausible, but qualitative, picture of the earthquake nucleation process.

The present study confirms and expands upon the earlier results of Dieterich (1986) that were based on numerical solutions of a single spring and slider approximation of a fault patch. It is found that the displacement history and time to instability for the simple model are not significantly different from the numerical results, including models that employ heterogeneity of fault stresses. The solutions presented above are for the simple case, in which the stress is applied to some level, followed by stressing at a constant rate. However, it is worth noting that these solutions may be applied, piecewise, to follow complicated stressing histories.

A characteristic interval of self-driven, accelerating fault creep, in the nucleation zone, leads to slip instability. This accelerating creep occurs in the stress interval between the steady-state friction, μ_s, and the maximum friction, μ_{max}. The principal new finding from the numerical model is the spontaneous development of a localized zone, or sub-patch, on which slip most rapidly accelerates. The dimensions of the sub-patch appear to scale by the relation for l_c (eq. 15). If conditions on the sub-patch are well removed from steady state, the appropriate scaling follows l_c obtained using $\xi \approx 0.4B$.

The curves of Figure 8, obtained with finite stressing rates, illustrate an interesting transition in the dependence of the time to instability on stress. At low stresses, below steady-state friction, changes in stress result in approximately linear changes in the time to instability. However, as the stress increases relative to the steady-state boundary, the dependence of time to instability on stress undergoes a transition to a linear dependence of the logarithm of the time to instability. From eq. 27, and as noted by Dieterich (1986), the slope of stress vs. ln t_i equals $-A$. This slope is also approximately obtained using the alternative evolution equation (Fig. 9), suggesting this property is insensitive to details of the evolution law employed.

The duration of the nucleation process can be quite long. For example, the time-to-instability solution at zero stressing rate (eq. 27) intercepts the μ_s line at t_i approaching θ (see Fig. 8). Recall, from evolution equation 5, that if the fault has remained fully locked, θ is equal to the elapsed time from the last earthquake.

These results suggest a picture of earthquake occurrence in which a seismic region has a continuous supply of sub-patches to nucleate earthquakes. These sub-patches form and evolve from the heterogeneity of conditions and local stress build-up. At any given time there will be numerous sub-patches that are at various stages of the localized slip acceleration process. The stressing

history experienced by a sub-patch might ideally consist of a constant background stressing rate, punctuated by stress steps at the time of nearby earthquakes. Because of the logarithmic dependence of the time to instability on stress in the later stages of the nucleation process, the timing of earthquakes will be very sensitive to perturbations of the stressing history. As discussed by Dieterich (1986) a population of patches that yields a constant rate of seismicity under constant stressing rate, will, following a step increase of stress, produce a higher rate of earthquakes that decays by the $1/t$ Omori law of aftershock decay. A paper is in preparation that applies the solutions presented here to the effects of stressing history on seismicity rates.

The result yielding a minimum patch dimension for unstable slip appears similar in many respects to the familiar fracture mechanics result for critical crack length for unstable crack growth. In each case, there is minimum crack size for instability, and in each case, if the crack is less than the critical size, an instability can occur only if crack grows to the critical dimension. Also, the rate- and state-dependent constitutive law yields a rate-dependent apparent fracture energy for initiation of slip at a crack tip that is analogous to the rate-dependent fracture energy for sub-critical growth of tensile fractures.

However, there are fundamental differences between the frictional and crack growth instabilities that appear to be of importance for applications to earthquake nucleation. The unstable crack solutions assume constant stress on the walls of the crack and fracture energy at the crack tip controls crack elongation. Conversely, for the nucleation of frictional instability, described here, the stress does not remain constant on slipping surfaces. Instability is controlled by rate- and state-dependent resistance to slip on the entire slipping fault patch. In the former case, instability pertains to crack growth, while in the latter, instability pertains to slip rate. A slip instability can occur under conditions of constant stiffness which is equivalent to instability on a patch of fixed size. The numerical models indeed demonstrate that slip instability can develop as the most active portion of the patch is constricting—a result that is not anticipated from fracture mechanics treatments.

Okubo (1989) employed the author's computer code and approach for quasi-static nucleation, described above, with a code for dynamic rupture propagation, to simulate the full earthquake cycle on a fault with rate- and state-dependent friction. The transition from quasi-static accelerating creep to earthquake rupture was accomplished by using the nodal stress, slip, slip speed and state from the final static time-step calculation as the starting point of the dynamic calculation. Okubo found that for the dynamic calculations, slip accelerated smoothly and spontaneously from the quasi-static solutions to initiate essentially crack-like dynamic rupture propagation. For the initial stages of the dynamic calculation, Okubo observes: "Once the critical fault patch is established, the rate of rupture extension quickly reaches the Rayleigh wave speed."

Similar results for the initial stages of dynamic rupture growth are reported for stick-slip experiments (Dieterich, 1980; Okubo and Dieterich, 1984; Okubo and Dieterich, 1986; Ohnaka et al., 1986; Ohnaka and Kuwahara, 1990). Those experiments show that in the interval beginning about 1 ms prior to rapid rupture propagation (speeds > 1 km/s), slip in the nucleation zone accelerates and spreads, but at significantly slower rupture speeds. The slip rates during this phase are characteristically in the range of 2–10 mm/s. Normalized by D_c, these slip speeds are roughly $\geqslant 1 \times 10^3 D_c$/s, which is beyond the cutoff speed for the quasi-static analysis reported here. Detailed experimental data for the much earlier quasi-static phase of nucleation considered in this study, when the numerical models predict that the zone of rapid slip constricts, do not appear to be available.

The development of a characteristic dimension of the nucleation zone prior to instability, and solutions for displacement on the patch, may provide some constraints on the moment $M_0 = (G\delta)$ (area) of premonitory slip. From the displacements given by eq. 23 and assuming the zone of accelerating slip forms a circular patch

with radius given by eq. 15, the moment in the interval t_1 before the instability to t_2 before instability is:

$$M_0 = \frac{G^3\pi\eta^2 A D_c^3}{(B-\xi)\xi\sigma^2} \ln\left[\frac{\frac{AD_c}{(B-\xi)\dot{\delta}_1} + t_1}{\frac{AD_c}{(B-\xi)\dot{\delta}_1} + t_2}\right] \quad (34)$$

Figure 11 plots eq. 34 for the interval t_1 = 10,000 s before instability to t_2 = 10 s before instability, using representative values for the parameters as given in the figure caption. Figure 11 illustrates the dependency of premonitory strain changes in the nucleation zone to the characteristic displacement D_c.

Based on laboratory measurements of D_c, Dieterich (1986) noted that strain from premonitory creep in the nucleation zone might be very difficult to detect as an earthquake precursor. In Figure 11, using D_c of 5×10^{-5} m, which is near the upper limit of the laboratory observations, the expected radius of the nucleation zone is small, 20 m or less, and the moment of premonitory slip is 10^{10} Nm or less. Johnston et al. (1987) report a failure to observe evidence of premonitory strain prior to moderate earthquakes that occurred near high-resolution borehole strain meters. The upper limit of strain precursors that would escape detection in their observations was about 10^{12} Nm, which is consistent with the conclusion based on laboratory observations of D_c. However, the scaling of D_c to faults in nature remains an open question. In the laboratory, D_c varies with surface roughness and gouge particle size, but the experiments cover a relatively narrow range of conditions.

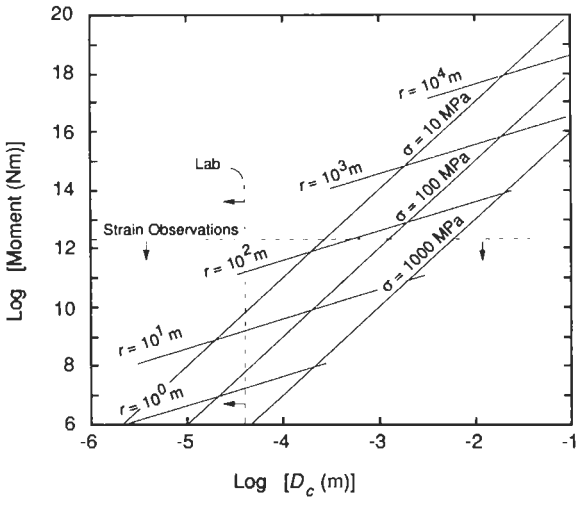

Fig. 11. Log_{10} of the moment of premonitory slip in the interval from 10,000 s from instability to 10 s before instability from eq. 34. Parameters used for this plot are: $A = 0.005$, $B = 0.007$, $\xi = 0.4B$, $\eta = 3\pi/24$, $G = 15{,}000$ MPa, and $\dot{\delta}_1 = 0.01$ m/s. Contours of r give the radius of the nucleation zone (from eq. 15). The dashed vertical line, with arrows, shows the approximate upper limit of D_c observed in laboratory experiments. The dashed horizontal line, with arrows, gives the approximate lower limit for detection of precursory strain signals from the earthquakes reported on by Johnston et al. (1987).

Acknowledgements

I wish to thank Paul Okubo and Paul Segall for useful suggestions and discussions in the early phases of this study. Reviews and comments on the manuscript by Paul Segall, Michael Blanpied, Vladimir Dubrovsky and T. Yamashita are greatly appreciated.

References

Biegel, R.L., Sammis, C.G. and Dieterich, J.H., 1989. The frictional properties of a simulated gouge with a fractal particle distribution. J. Struct. Geol., 11: 827–846.

Blanpied, M.L. and Tullis, T.E., 1986. The stability and behavior of a frictional system with a two state variable constitutive law. Pure Appl. Geophys., 124: 415–444.

Chinnery, M.A., 1969. Theoretical fault models. In: K. Kasahara and A.E. Stevens (Editors), A Symposium on Processes in the Focal Region. Publications of the Dominion Observatory, Ottawa, Canada Department of Energy, Mines and Resources, Ottawa, 37, No. 7, pp. 211–223.

Dieterich, J.H., 1978. Time-dependent friction and the mechanics of stick-slip. Pure Appl. Geophys., 116: 790–806.

Dieterich, J.H., 1979. Modeling of rock friction, 1. Experimental results and constitutive equations. J. Geophys. Res., 84: 2161–2168.

Dieterich, J.H., 1980. Experimental and model study of fault constitutive properties. In: S. Nemat-Nasser (Editor), Solid Earth Geophysics and Geotechnology. AMD 42, American Society of Mechanical Engineers, New York, N.Y., pp. 103–120, 21–29.

Dieterich, J.H., 1981a. Constitutive properties of faults with simulated gouge. In: N.L. Carter, M. Friedman, J.M. Logan and D.W. Stearns (Editors), Mechanical Behavior of

Crustal Rocks. Am. Geophys. Union, Geophys. Monogr., 24: 103–120.

Dieterich, J.H., 1981b. Potential for geophysical experiments in large scale tests. Geophys. Res. Lett., 8: 653–656.

Dieterich, J.H., 1986. A model for the nucleation of earthquake slip. In: S. Das, J. Boatwright and C.H. Scholz (Editors), Earthquake Source Mechanics. Am. Geophys. Union, M. Ewing Vol. 6, Geophys. Monogr., 37: 37–47.

Dieterich, J.H., 1987. Nucleation and triggering of earthquake slip: effect of periodic stresses. Tectonophysics, 144: 127–139.

Dieterich, J.H., 1988. Nucleation of earthquakes on faults with rate and state dependent fault strength (abstr.). Trans. Am. Geophys. Union, EOS, 69, No. 44, p. 1423.

Dieterich, J.H. and Conrad, G., 1984. Effect of humidity on time- and velocity-dependent friction in rocks. J. Geophys. Res., 89: 4196–4202.

Eshelby, J.D., 1957. The determination of the elastic field of an ellipsoidal inclusion, and related problems. Proc. R. Soc. London, A, 241: 376–396.

Gu, J.-C., Rice, J.R., Ruina, A.L. and Tse, S.T., 1984. Slip motion and stability of a single degree of freedom elastic system with rate and state dependent friction. J. Mech. Phys. Solids, 32: 167–196.

Johnston, M.J.S., Linde, A.T., Gladwin, M.T. and Borcherdt, R.D., 1987. Fault failure with moderate earthquakes. Tectonophysics, 144: 189–206.

Knopoff, L., 1958. Energy release in earthquakes. Geophys. J., 1: 44–52.

Koslov, D.D. and Liu, H.P., 1980. Reformulation and discussion of mechanical behavior of the time-dependent friction law proposed by Dieterich. Geophys. Res. Lett., 7: 913–916.

Ohnaka, M. and Kuwahara, Y., 1990. Characteristic features of local breakdown near a crack-tip in the transition zone from nucleation to unstable rupture during stick-slip shear failure. Tectonophysics, 175: 197–220.

Ohnaka, M., Kuwahara, Y., Yamamoto, K. and Hirasawa, T., 1986. Dynamic breakdown processes and the generating mechanism for high-frequency elastic radiation during stick-slip instabilities. In: S. Das, J. Boatwright and C.H. Scholz (Editors), Earthquake Source Mechanics. Am. Geophys. Union, M. Ewing Vol. 6, Geophys. Monogr., 37: 13–24.

Okubo, P.G., 1989. Dynamic rupture modeling with laboratory derived constitutive relations. J. Geophys. Res., 94: 12321–12336.

Okubo, P.G. and Dieterich, J.H., 1984. Effects of physical fault properties on frictional instabilities produced on simulated faults. J. Geophys. Res., 89: 5817–5827.

Okubo, P.G. and Dieterich, J.H., 1986. State variable fault constitutive relations for dynamic slip. In: S. Das, J. Boatwright and C.H. Scholz (Editors), Earthquake Source Mechanics. Am. Geophys. Union, M. Ewing Vol. 6, Geophys. Monogr., 37: 25–35.

Rice, J.R. and Gu, J.-C., 1983. Earthquake aftereffects and triggered seismic phenomena. Pure Appl. Geophys., 121: 187–219.

Rice, J.R. and Ruina, A.L., 1983. Stability of steady frictional slipping. Trans. ASME, J. Appl. Mech., 50: 343–349.

Ruina, A.L., 1980. Friction Laws and Instabilities: A Quasistatic Analysis of Some Dry Friction Behavior. Ph.D. Thesis, Brown University, Providence, R.I.

Ruina, A.L., 1983. Slip instability and state variable friction laws. J. Geophys. Res., 88: 10359–10370.

Ruina, A.L., 1985. Constitutive laws for frictional slip. In: Mechanics of Geomaterials. Wiley, New York, pp. 169–187.

Starr, A.T., 1928. Slip in a crystal and rupture in a solid due to shear. Proc. Cambridge Philos. Soc., 24: 489–500.

Stuart, W.D., 1988. Forecast model for great earthquakes at the Nankai trough subduction zone. Pure Appl. Geophys., 126: 619–641.

Tse, S.T. and Rice, J.R., 1986. Crustal earthquake instability in relationship to the depth variation of frictional slip properties. J. Geophys. Res., 91: 9452–9472.

Tullis, T.E. and Weeks, J.D., 1986. Constitutive behavior and stability of frictional sliding of granite. Pure Appl. Geophys., 124: 383–314.

Weeks, J.D. and Tullis, T.E., 1985. Frictional sliding of dolomite: a variation in constitutive behavior. J. Geophys. Res., 90: 7821–7826.